Fluid–structure interaction of free convection in a square cavity divided by a flexible membrane and subjected to sinusoidal temperature heating

Received 29 December 2018
Revised 22 February 2019
Accepted 25 February 2019

Mohammad Ghalambaz
School of Aeronautic Science and Engineering, Beihang University, Beijing, China and Department for Management of Science and Technology Development, Ton Duc Thang University, Ho Chi Minh City, Vietnam

S.A.M. Mehryan
Young Researchers and Elite Club, Yasooj Branch, Islamic Azad University, Yasooj, Iran

Muneer A. Ismael
Department of Mechanical Engineering, Engineering College, University of Basrah, Basrah, Iraq

Ali Chamkha
Department of Mechanical Engineering, Prince Mohammad Bin Fahd University, Al-Khobar, Saudi Arabia, and

D. Wen
School of Aeronautic Science and Engineering, Beihang University, Beijing, China and School of Chemical and Process Engineering, University of Leeds, Leeds, UK

Abstract

Purpose – The purpose of the present paper is to model a cavity, which is equally divided vertically by a thin, flexible membrane. The membranes are inevitable components of many engineering devices such as distillation systems and fuel cells. In the present study, a cavity which is equally divided vertically by a thin, flexible membrane is model using the fluid–structure interaction (FSI) associated with a moving grid approach.

Design/methodology/approach – The cavity is differentially heated by a sinusoidal time-varying temperature on the left vertical wall, while the right vertical wall is cooled isothermally. There is no thermal diffusion from the upper and lower boundaries. The finite-element Galerkin technique with the aid of an arbitrary Lagrangian–Eulerian procedure is followed in the numerical procedure. The governing equations are transformed into non-dimensional forms to generalize the solution.

Findings – The effects of four pertinent parameters are investigated, i.e., Rayleigh number ($104 = Ra = 107$), elasticity modulus ($5 \times 1012 = E_T = 1016$), Prandtl number ($0.7 = Pr = 200$) and temperature oscillation frequency ($2p = f = 240p$). The outcomes show that the temperature frequency does not induce a notable effect

The work was supported by National Numerical Windtunnel (Grant 2018-ZT3A05) and 111 project (B18002). The second author acknowledges the Young Researchers and Elite Club, Yasooj Branch, Islamic Azad University, Yasooj, Iran, for its financial support.

International Journal of Numerical Methods for Heat & Fluid Flow
Vol. 30 No. 6, 2020
pp. 2883-2911

0961-5539
DOI 10.1108/HFF-12-2018-0826

on the mean values of the Nusselt number and the deformation of the flexible membrane. The convective heat transfer and the stretching of the thin, flexible membrane become higher with a fluid of a higher Prandtl number or with a partition of a lower elasticity modulus.

Originality/value – The authors believe that the modeling of natural convection and heat transfer in a cavity with the deformable membrane and oscillating wall heating is a new subject and the results have not been published elsewhere.

Keywords Convection heat transfer, Fluid–structure interaction (FSI), Flexible membrane, Sinusoidal temperature

Paper type Research paper

Nomenclature

$\boldsymbol{d}_s$ = vector of displacement;
E = Young's modulus in dimensional form;
E_τ = elasticity modulus in non-dimensional form;
f = frequency;
$\boldsymbol{F}_v$ = vector of body force;
g = vector of gravitational acceleration;
L = size of the cavity;
n = number of periods;
n_i = normal direction to the flexible separator;
P = fluid pressure;
Pr = Prandtl number;
Ra = thermal Rayleigh number;
t = dimensional time;
T = temperature;
T_p = period of oscillation;
$\boldsymbol{u}$ = vector of velocity;
$\boldsymbol{w}$ = velocity vector of the moving grid;
x = Cartesian coordinate in x-direction; and
y = Cartesian coordinate in y-direction.

Greek symbols

α = thermal diffusivity;
β = volumetric thermal expansion coefficient;
σ = Tensor of stress;
τ = non-dimensional time;
μ = dynamic viscosity;
ν = Poisson's ratio;
ρ = density; and
ρ_R = density ratio of fluid-to-solid structure.

Subscripts

av = average;
c = cold temperature;
f = fluid;

h = hot temperature;
p = membrane partition; and
s = membrane domain (solid).

Subscripts

* = indicates the dimensional parameter.

1. Introduction

Membranes are an inevitable part of many engineering devices such as distillation (Cassard and Park, 2018), filtration (Feng *et al.*, 2017), fuel cells (Jang *et al.*, 2018) and separator (Xie *et al.*, 2016) systems. Moreover, many engineering applications have promoted the problem of natural convection inside enclosures, which has attracted intensive research interest. Baïri *et al.* (2014) reviewed the applications of free convection in enclosures by explaining the different solutions to treat natural convection phenomena. The study demonstrated the importance of natural convection in enclosures.

Moreover, the natural convection in porous pores, fuel cells, buildings and insulation of heat storage systems can be modeled as a cavity. The cavities have been extensively studied in previous and recent studies owing to its important engineering applications. Different characteristics of convection heat transfer were studied to improve or control the heat transfer process in homogeneous cavities (Tahmasebi *et al.*, 2018; Sheikholeslami *et al.*, 2019; Mehryan *et al.*, 2019), cavity with MHD effects (Sadiq *et al.*, 2018; Alsabery *et al.*, 2018b, Bondareva and Sheremet, 2018), conjugate heat transfer (Alsabery *et al.*, 2018a, Alsabery *et al.*, 2017), layered cavities (Ghalambaz *et al.*, 2018; Mehryan *et al.*, 2019b, Sheremet *et al.*, 2018; Miroshnichenko *et al.*, 2018), cavity with obstacles (Alsabery *et al.*, 2019; Abouali and Falahatpisheh, 2009; Astanina *et al.*, 2018; Bondarenko *et al.* (2019), Alsabery *et al.*, 2018d), in partitioned cavities such as a cavity partially filled with a layer of porous media (Chamkha and Ismael, 2014; Mehryan *et al.*, 2019), diagonally divided square cavity (Varol *et al.*, 2009), gas chamber divided by a permeable membrane (de Almeida and Hart, 2017), a cavity with an off-center partition (Tatsuo *et al.*, 1987), a cavity with multiple vertical partitions (Nishimura *et al.*, 1988), a vertically divided cavity (Oztop *et al.*, 2009), divided cavities with various thermal boundary conditions (Oztop *et al.*, 2009), a partitioned cavity subject to a uniform heat flux (Kahveci, 2007) and partitioned cavities with various thermal boundary conditions (Xu *et al.*, 2009; Kalabin *et al.*, 2005; Küttler and Wall, 2008).

Flow-through devices incorporated with diaphragms like pump and sensors, flow-through flexible conduits and reciprocating pistons or fluid splashing in containers of flexible wall (Engel and Griebel, 2006) are deformable-domain problems. The most efficient and robust numerical method developed in such problems is the arbitrary Lagrangian–Eulerian method (ALE) (van Loon *et al.*, 2007). Fu and Huang (2006) straddled this numerical approach to study the free convection in a vertical channel containing a vibrated surface. They found lesser convection effect compared with a stationary surface. Lee *et al.* (2012) investigated the impact of the elasticity property of flapping wings on the thrust generation. They indicated a major role of the modulus of elasticity on the drag exerted by the flow. Mehryan *et al.* (2019a) investigated the mixed-convection flow of induced by oscillating of a cylinder in a cavity using the ALE approach.

Kalmbach and Breuer (2013) have provided experimental reference data regarding the fluid–structure interaction (FSI) benchmark case under turbulent flow conditions. Their structure consisted of a rigid cylinder tailed with a para-rubber sheet acting as a splitter.

At the end of the para-rubber sheet, a mass was attached to reduce the flutter effect. They found the flexible splitter reduced the drag of flow compared with a rigid splitter. De Nayer and Breuer (2014) utilized the FSI experiments of (Kalmbach and Breuer, 2013) along with the large-eddy simulation to show that the modulus of elasticity of rubber had an essential effect on the FSI phenomenon. Ghalambaz *et al.* (2017) and Alsabery *et al.* (2018c) used the ALE approach to study the effect of an oscillating-fin on the convective heat exchange in a differentially heated cavity. The oscillating fashion of the fin did not overcome its drag action. Therefore, they recognized the deterioration of the heat exchange despite the mixing effect introduced by the fin.

Very recently, Jamesahar *et al.* (2016) and Mehryan *et al.* (2017b) considered the free convection in cavities subdivide by flexible membrane by studying the fluid–solid interaction between free convection and membrane. Jamesahar *et al.* (2016) showed that the reformable cavities affected the rate of heat exchange compared with a rigid partition. The results of Mehryan *et al.* (2017b) confirmed that the fluid interaction with the solid significantly influenced the shape of a very thin, flexible partition (membrane). Studies of both Jamesahar *et al.* (2016) and Mehryan *et al.* (2017b) concluded that the deformable membrane could influence the flow and heat patterns in the cavity. Therefore, both fluid and structure were coupled and should be solved simultaneously. In both studies (Mehryan *et al.*, 2017b, Jamesahar *et al.*, 2016), the cavities were differentially heated. However, in many real applications, imposing the perfectly constant wall temperature is hard to be attained. Practically, the wall temperature fluctuates about a range of temperature with a periodic fluctuation frequency. By careful study of the physics of a cavity containing a flexible partition, it can be inferred that the transient effect of heat exchange could be very important because the free convective flow is the result of the temperature difference (buoyancy forces). The membrane also affects the flow owing to its interaction with the fluid. In a cavity with a membrane, imposing a transient thermal boundary condition to the cavity walls produces a transient flow and heat exchange together with a transient shape of the membrane. For low frequencies of temperature fluctuations, the variation in the shape of the membrane may follow the induced thermal patterns (De Nayer and Breuer, 2014). However, for moderate frequencies of the temperature fluctuations, the response time of the membrane could not be as fast as the induced changes in the flow and heat patterns, and hence, the membrane could also act as a filter medium for temperature and flow fluctuations in the cavity.

The membranes are very thin, and hence, in many applications, the interaction of the fluid and the membrane can easily change the shape of the membrane. The change in the shape of the membrane would also change the flow and heat transfer mechanism. The present study aims to point out a novel approach, the FSI approach, associated with a moving grid domain to model the deformation of a membrane owing to the interaction with a fluid flow. This paper is a sequel to the author's work (Mehryan *et al.*, 2017b) on a cavity subdivided by a partition. The main novelty of the current paper is that we imposed two fundamental intrinsic matters: the first is that a cyclic thermal boundary condition heats the cavity and the second is the effect of a wide range of Prandtl number. These two effects are important in the modeling of fuel cells and the separators, in which the membrane acts as the selective layer and is exposed to fluid flow.

2. Mathematical modeling

A view of the geometry of the considered problem is shown schematically in Figure 1 along with the coordinate system and imposed boundary conditions. The dimensions of the enclosure in x^*, y^* coordinates are so much higher than the dimensions in z^*. Accordingly, a

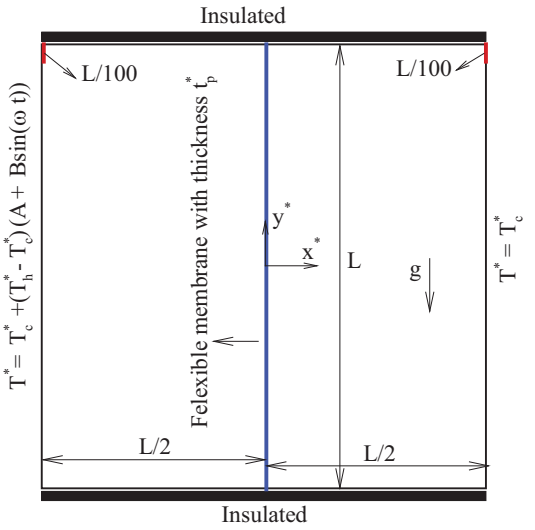

Figure 1.
Physical problem and coordinate system

two-dimensional scope of the geometry can correctly model the problem. The heat source associated with the hot bound imposes a time-periodic temperature so that $T^* = T_c^* + \left(T_h^* - T_c^*\right)(A + Bsin(\omega t))$, while the opposite cold one has the uniform temperature of T^*_c. The lower and upper bounds of the enclosure are thermally impervious. A thin, flexible membrane is used to partition the enclosure into two smaller ones. The thickness of the membrane is t_p^*. The fluid filling the enclosures behaves as an incompressible and Newtonian one. The boundary condition of time-periodic temperature on the left bound necessitates that the flow is unsteady. The present buoyancy-driven flow applies the Boussinesq approximation. This approximation neglects the variations of density except where they are in terms containing the gravity acceleration. Because the flexible separator is thin and with low thermal resistance, the gradient of temperature in it is zero.

Two eyelets of $L/100$ height are located on the top of the vertical bounds, while the other bounds and the flexible membrane are impervious against the mass flow. The goal of the eyelets is to control the fluid flow. The eyelets are considered very small, and hence, the only effect of these eyelets is to balance the pressure in the two sides of the cavity. The densities of the fluid and the flexible membrane are the same. The flexible divider behaves as a hyperelastic material reacting non-linearly against the imposed forces by the fluid.

2.1 Fluid–structure interaction model

Description of the correlative effects of the fluid and deformable solid material is performed by the known technique of the Arbitrary Lagrangian-Eulerian (ALE). The fluid flow within the enclosure is portrayed by the incompressible mass conservation and the linear momentum equations for the pressure and velocity fields (Mehryan *et al.*, 2017a, Zargartalebi *et al.*, 2018):

$$\nabla^* \cdot \boldsymbol{u}^* = 0 \tag{1}$$

$$\frac{\partial \boldsymbol{u}^*}{\partial t} + (\boldsymbol{u}^* - \boldsymbol{w}^*) \cdot \nabla^* \boldsymbol{u}^* = -\frac{1}{\rho_f} \nabla^* P^* + v_f \nabla^{*2} \boldsymbol{u}^* + \beta \boldsymbol{g} (T^* - T_c^*) \tag{2}$$

Also, the energy equation which describes the temperature field can be represented as follows (Zargartalebi *et al.*, 2018):

$$\frac{\partial T^*}{\partial t} + (\boldsymbol{u}^* - \boldsymbol{w}^*) \cdot \nabla^* T^* = \alpha_f \nabla^{*2} T^* \tag{3}$$

The structural deformations of the flexible membrane can be achieved by the following nonlinear geometric and elastic formulation (Mehryan *et al.*, 2017b):

$$\rho_s \frac{d^2 \boldsymbol{d}_s^*}{dt^2} - \nabla^* \boldsymbol{\sigma}^* = \boldsymbol{F}_v^* \tag{4}$$

$\boldsymbol{F}_v^*$ of the above-written equation is the applied volume forces on the deformable membrane, $\boldsymbol{\sigma}^*$ is the solid stress tensor, $\boldsymbol{d}_s^*$ is the displacement vector of moving coordinate system so that $d\boldsymbol{d}_s^*/dt = \boldsymbol{w}^*$ and ρ_s is the density of the membrane.

In this study, the neo-Hookean solid model has been used for assigning the stress tensor $\boldsymbol{\sigma}^*$ (Ogden, 1997). This model is applied to characterize the stress–strain nonlinear behavior of a hyperelastic material with large deformations (Ogden, 1997). The hyper-elastic theory is used more for modeling of rubbery behavior of a polymeric material and polymeric foams that can have large deformations. The model can be written as follows (Jamesahar *et al.*, 2016):

$$\boldsymbol{\sigma}^* = J^{-1} F S F^{tr} \tag{5a}$$

where:

$$F = \left(I + \nabla^* \boldsymbol{d}_s^*\right), J = det(F) \text{ and } S = \partial W_s / \partial \boldsymbol{\varepsilon} \tag{5b}$$

are the deformation gradient, the determinant of the matrix F and the partial differential of the density function of strain energy. Also, the density function of the strain energy W_s and strain $\boldsymbol{\varepsilon}$ is defined through the equations (6) and (7) (Jamesahar *et al.*, 2016):

$$W_s = \frac{1}{2} \mu_l \left(J^{-1} I_1 - 3\right) - \mu_l \ln(J) + \frac{1}{2} \lambda (\ln(J))^2 \tag{6}$$

$$\boldsymbol{\varepsilon} = \frac{1}{2} \left(\nabla^* \boldsymbol{d}_s^* + \nabla^* \boldsymbol{d}_s^{*tr} + \nabla^* \boldsymbol{d}_s^{*tr} \nabla^* \boldsymbol{d}_s^*\right) \tag{7}$$

λ and μ_l of the above equations, known as Lame's first and second constants, respectively, are related to Poisson's coefficient and elasticity module using $\mu_l = E/2(1+v)$, and $\lambda = Ev/(1+v)(1-2v)$. I_1 is called the first constant of the deformation tensor.

2.2 Boundary conditions

All the bounds of the enclosure are motionless ($u^* = v^* = 0$). The lower and topper bounds of both sub-cavities are thermally insulated ($\partial T^*/\partial y^* = 0$). The right-hand wall is at a constant

temperature $T^* = T_c^*$, while a time-sinusoidal function of temperature is imposed on the left-hand wall such that its period-averaged value is $A\left(T_h^* - T_c^*\right) + T_c^*$. This function is written in the term $T^* = T_c^* + \left(T_h^* - T_c^*\right)(A + Bsin(\omega t))$, where ω shows the oscillation frequency, and values of A and B are 1 and 0.1, respectively.

Along the FSI, continuity of the dynamic motion and kinematic forces are the boundary conditions used to model the fluid and deformable membrane interaction. These conditions can be represented as:

$$\frac{\partial \boldsymbol{d}_s^*}{\partial t} = \boldsymbol{u}^* \text{ and } \boldsymbol{\sigma}^* \cdot n_i^* = -P^* + \mu_f \nabla^* \boldsymbol{u}^* \tag{8}$$

Applying the conservation of energy on the flexible membrane along with the previous assumptions results in equation (9) as follows:

$$\frac{\partial T^{*+}}{\partial n_i^*} = \frac{\partial T^{*-}}{\partial n_i^*} \tag{9}$$

In this equation, the plus and minus symbols denote the right and left sides of the deformable membrane, respectively. Also, the boundary condition for both eyelets can be represented as follows:

$$\left[-P^* + \mu_f \nabla^* \boldsymbol{u}^*\right] \cdot n_i^* = 0 \tag{10}$$

2.3 Non-dimensional form of governing equations

To provide with dimensions, non-dimensional parameters are introduced as follows:

$$\boldsymbol{d}_s = \frac{\boldsymbol{d}_s^*}{L}, \boldsymbol{\sigma} = \frac{\boldsymbol{\sigma}^*}{E}, \tau = \frac{t\alpha_f}{L^2}, (x, y, n_i) = \frac{\left(x^*, y^*, n_i^*\right)}{L} \tag{11a}$$

$$\boldsymbol{u} = \frac{\boldsymbol{u}^* L}{\alpha_f}, \boldsymbol{w} = \frac{\boldsymbol{w}^* L}{\alpha_f}, P = \frac{L^2}{\rho_f \alpha_f^2}, T = \frac{T^* - T_c^*}{T_h^* - T_c^*} \tag{11b}$$

$$\nabla = \frac{\nabla^*}{1/L}, \nabla^2 = \frac{\nabla^{*2}}{1/L^2}, t_p = \frac{t_p^*}{L} \tag{11c}$$

To dimensionalize the equations, the above parameters are substituted for the equations (1)-(4). Therefore, we have:

$$\frac{1}{\rho_R} \frac{d^2 \boldsymbol{d}_s}{d\tau^2} - E_\tau \nabla \boldsymbol{\sigma} = E_\tau \boldsymbol{F}_v \tag{12}$$

$$\nabla \cdot \boldsymbol{u} = 0 \tag{13}$$

$$\frac{\partial \boldsymbol{u}}{\partial \tau} + (\boldsymbol{u} - \boldsymbol{w}) \cdot \nabla \boldsymbol{u} = -\nabla P + Pr\nabla^2 \boldsymbol{u} + Pr\boldsymbol{Ra}T \tag{14}$$

$$\frac{\partial T}{\partial \tau} + (\boldsymbol{u} - \boldsymbol{w}) \cdot \nabla T = \nabla^2 T \tag{15}$$

where:

$$\boldsymbol{Ra} = \frac{\boldsymbol{g}\beta\left(T_h^* - T_c^*\right)L^3}{\upsilon_f \alpha_f}, Pr = \frac{\upsilon_f}{\alpha_f}, E_\tau = \frac{EL^2}{\rho_f \alpha_f^2}, \boldsymbol{F}_v = \frac{(\rho_f - \rho_s)L\boldsymbol{g}}{E}, \rho_R = \frac{\rho_f}{\rho_s} \tag{16}$$

The vectors of $\boldsymbol{Ra}$ and $\boldsymbol{F_v}$ act in the direction of the y-axis, upwards and downwards, respectively. Since the Rayleigh number includes the vector of gravity acceleration, it has been represented as a vector. Indeed, the Rayleigh numbers in the x and y directions are zero and $Ra = |\boldsymbol{Ra}|$, respectively.

Finally, the non-dimensional forms of the velocities and temperatures on the bounds are:

$$x = 0, y: u = v = 0 \text{ and } T = A + B\sin(f\tau) \tag{17a}$$

$$x = 1, y: u = v = 0 \text{ and } T = 0 \tag{17b}$$

$$y = 0, x: u = v = 0 \text{ and } \partial T/\partial y = 0 \tag{17c}$$

$$y = 1, x: u = v = 0 \text{ and } \partial T/\partial y = 0 \tag{17d}$$

For the fluid–membrane (solid) interface:

$$\begin{cases} E_\tau \boldsymbol{\sigma} \cdot n_i = -P + \mathrm{Pr}\nabla \boldsymbol{u} \\ \partial \boldsymbol{d}_s/\partial \tau = \boldsymbol{u} \\ T^+ = T^-, \partial T^+/\partial n_i = \partial T^-/\partial n_i \end{cases} \tag{17e}$$

For both of the eyelets:

$$[\mathrm{Pr}\nabla \boldsymbol{u} - P] \cdot n_i = 0 \tag{17f}$$

where the dimensionless frequency of the periodic temperature is defined as $f = \omega L^2/\alpha_f$. Here, two definitions are expressed to evaluate the rate of heat transfer: first, the average Nusselt number along with the left- or the right-side walls at a specified time is:

$$Nu_{av} = -\int_0^1 \frac{\partial T}{\partial x} dy \tag{18}$$

Secondary, the average Nusselt number in one period is defined as:

$$Nu_{av,T_p} = -\int_{nT_p}^{(n+1)T_p} \int_0^1 \frac{\partial T}{\partial x} dy d\tau \tag{19}$$

where n and T_p are the number of periods and the period, respectively. Also, the dimensionless mean temperature in the whole enclosure is calculated as follows:

$$T_{av} = \frac{\int_A T_{local} dA}{\int_A dA} \tag{20}$$

Here, A denotes the domain of the enclosure. To describe the fluid flow inside the sub-cavities, the concept of the stream function can be used as follows:

$$u = \frac{\partial \psi}{\partial y} \text{ and } v = -\frac{\partial \psi}{\partial x} \tag{21}$$

3. Numerical method, grid independence test and validations

The interdependent, complex and non-linear equations (12)-(15) are solved by employing the Galerkin finite element approach with the aid of the ALE technique. The numerical approach of the finite element are expressed in Donea and Huerta (2003) and Basak and Chamkha (2012) in details. A mesh of non-uniform triangular elements is employed to discretize the computational domain. The three-point Gaussian quadrature with bi-quadratic functions were used for calculating the residuals. In each time step, the Newton–Raphson method was applied to iteratively solve the residual equations until they reach 10^{-5} or lower. Owing to the coupling of fluid and structure, using an adequate time step is very important. In the present study, the time step is controlled automatically using a free time step backward differentiation formula (BDF). The utilized BDF is of variable order (1-2) (Süli and Mayers, 2003).

For as much as the results of the numerical solutions depend on the number of grid cells, first, it must be proven that the results are independent of the grid size. In the present investigation, a grid independence test has been done. A grid independence study has been performed for the mean Nusselt number in a period of oscillation and the dimensionless temperature at Point A with the position of $x = 0.025$ and $y = 0$ next to the flexible bound when $Ra = 10^7$, $E_\tau = 10^{13}$, $Pr = 6.2$ and $f = 20\pi$. The increase of the Rayleigh number enhances the strength of the convection regime and reduces the thickness of the boundary layer which, as a result, boosts the gradients of the temperature and velocity in the vicinity of the enclosure walls. The increase of the stiffness of the membrane also increases the

tension gradients in the flexible structure. The Prandtl number of 6.2 is common in the literature, and it is close to the Prandtl number of water. The set of $Ra = 10^7$, $E_\tau = 10^{13}$ indicates the most sensitive case in the present study. Thus, the grid check has been performed for this set of non-dimensional variables.

Figure 2 shows the general and zoomed views of the selected grid. Figure 3 shows the temperature at the coordinate of Point A ($x = 0.025$, $y = 0$) for several meshes of different sizes. The results for Nusselt number are presented in Table I. The temperature time series of Point A are plotted in Figure 3. The outcomes show that the grid of size 11,406 elements is appropriate for the numerical simulation.

To ensure the accuracy of the current modeling and simulation, the used solution method has been used to resolve several problems investigated in the literature. In the first validation, the results obtained in this study and those by Xu *et al.* (2009) have been compared. Xu *et al.* (2009) have studied the heat transfer of transient free convection in an enclosure divided into two parts using a rigid partition. It is worth noting that in the work of Xu *et al.* (2009), the variable τ is defined as $\tau = t\alpha_f Ra^2/L^2$. It is evidently shown in Figure 4

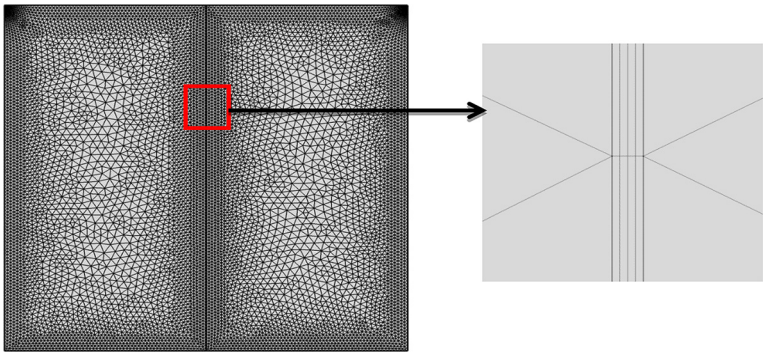

Figure 2.
General and zoom views of the grid selected

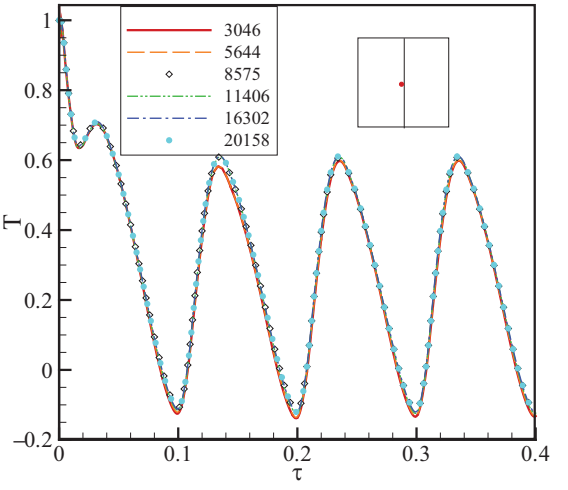

Figure 3.
Time series of the dimensionless temperature at Point A ($x = 0.025, y = 0$) obtained in different grids

that there is an excellent agreement between the outcomes of this work and those reported in (Xu *et al.*, 2009). This validation verifies the sufficiency of the present solution to simulate the transient natural convection in the fluid domain and the partition.

Another validation is the comparison of the deformation of the lower bound of a lid-driven enclosure computed by the present study and that computed by Küttler and Wall (2008). The schematic view of the study of Küttler and Wall (2008) along with the used physical values have been depicted inside (Figure 5). In Küttler and Wall (2008), the bottom bound was flexible, and the induced flow owing to the lid movements would change the configuration of the bound. From Figure 5, it can be observed that the current solution method is highly acceptable. This comparison confirms the capability of the present formulation and the solution for dealing with the FSI physics in an ALE system of meshing.

The last validation compares the experimental outcomes reported by Tatsuo *et al.* (1987) and the numerical results calculated of this investigation. Also, the validation compares our results and Churchill's relation (Churchill, 1983). As previously mentioned, Tatsuo *et al.* (1987) conducted experimental research on free convection in a regular quadrilateral divided vertically by N multiplex rigid plates. In the case of $N = 1$ and $Ar = 4$ (height/length), the study of Tatsuo *et al.* (1987) is very similar to the present study. From Figure 6, great accordance is established between the experimental outcomes and Churchill's relation. This comparison confirms the

cases	No. of elements	$Nu_{av,\,T_p}$	Average of error (%)*
1	3064	84.06	
2	5644	82.15	1.91
3	8575	81.45	0.70
4	11406	81.10	0.35
5	16302	80.74	0.36
6	20158	80.75	0.10

Note: *Error = $|Nu_{av,\,T_p,\,i+1} - Nu_{av,\,T_p,\,i}|/|Nu_{av,\,T_p,\,i}|$

Table I. Grid independency test for $Ra = 10^7$, $E_\tau = 10^{13}$, $f = 20\pi$ and $Pr = 6.2$

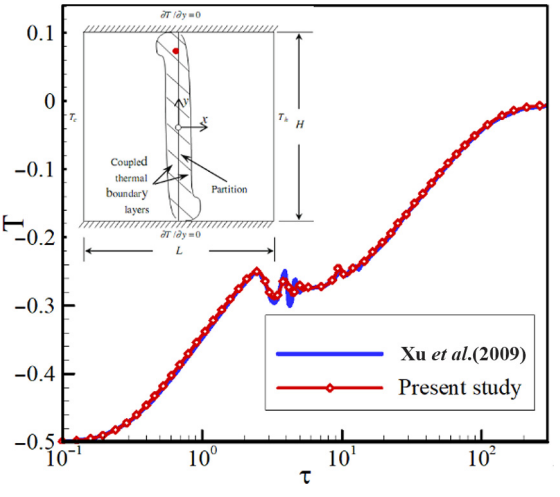

Figure 4. Comparison of the dimensionless temperature reported by Xu *et al.* (2009) and this study at a certain point (0.0083, 0.375)

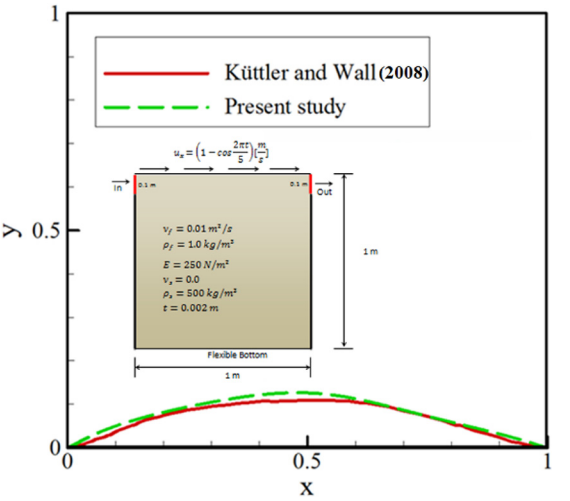

Figure 5.
Deformation of the flexible bottom wall of the lid-driven cavity perused by Küttler and Wall (2008) and the present study at $t = 7.5$ s

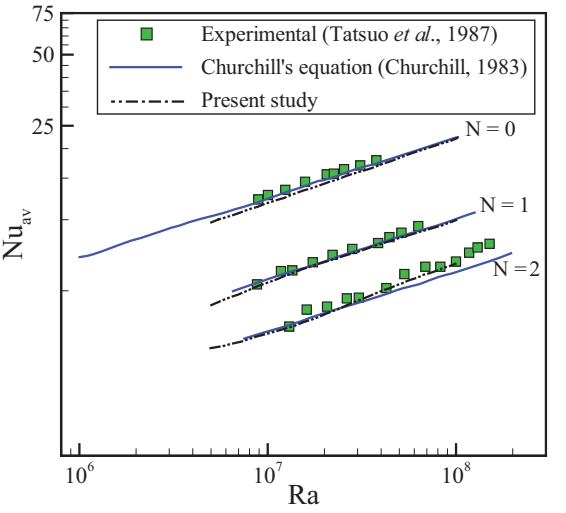

Figure 6.
Comparison of average Nusselt between the results of the present study and experimental results reported by Tatsuo *et al.* (1987) and Churchill's (1983) relation at $Pr = 6$ and $Ar = 4$

correctness of the results from the natural convection heat transfer point of view for the large values of τ where the convective heat transfer reaches to its steady state.

4. Results and discussion

Here, the impacts of the dimensionless parameters of Rayleigh number ($10^4 \leq Ra \leq 10^7$), elasticity modulus ($5 \times 10^{12} \leq E_\tau \leq 10^{16}$) and frequency ($2\pi \leq f \leq 40\pi$) on the rate of heat transfer, stress in the solid flexible partition and the patterns of the flow and temperature are investigated. This range of elasticity modulus is in agreement with

most of membrane and rubber materials. For instance, by assuming that the cavity is filled with water $\rho_f = 1{,}000\,\mathrm{kg/m^3}$, $\alpha_f = 0.155 \times 10^{-6}$, $L = 0.1$, and the membrane as rubber ($E = 0.01 \times 10^9$ to 0.1×10^9), the non-dimensional elasticity modulus parameter can be evaluated as $E_\tau = 4.2 \times 10^{15}$ to 4.2×10^{16}. The values considered for Prandtl number are 0.71, 6.2 and 200, which correspond to the working fluids of air, water and engine oil, respectively. As discussed by Markatos and Pericleous (1984), for a regular square cavity, the critical Rayleigh number starts from 10^6, and for a Rayleigh number higher than this value, the transient phenomenon can be expected. However, it should be noticed that the presence of the membrane, acting as a partition, suspends the commencing of the transient phenomenon to much higher Rayleigh numbers. For instance, Xu *et al.* (2009) addressed the heat transfer of laminar free convection in a square enclosure partitioned into two equal parts by a rigid partition for a Rayleigh number up to 9.2×10^8. More details regarding the range of non-dimensional values can be found in Ghalambaz *et al.* (2017) and Jamesahar *et al.* (2016).

4.1 Effects of Rayleigh number

In the current category, the dimensionless parameters E_τ, f and Pr are fixed at 10^{13}, 10π and 6.2, respectively, while the Rayleigh number Ra varies from 10^4 to 10^7. Figure 5 shows the streamlines for the mentioned range of Ra in different periods of oscillation. As envisaged, the maximum value of stream function $|\psi|_{max,}$ introduced as the intensity of the flow increases as Ra increases. This result is referred to the fact that an increase of Ra enhances the buoyancy force in the momentum equation. This effect can be seen in the four considered periods of oscillation. Besides, a single clockwise (CW) circulation (negative stream function) is formed in the cases of low Ra values ($Ra = 10^4$ and 10^5) in both sub-cavities. However, at high Ra numbers ($Ra = 10^6$ and 10^7), the CW vortex created in the right part of the enclosure becomes stronger, and as a result, it breaks up into two vortices. Hence, the fluid–solid interaction forces increase slowly until it deforms the impermeable flexible membrane to the left as shown in Figure. 7. It is worth mentioning that the streamlines get crowded close to the flexible membrane, which indicates an intensified flow there. Besides, at lower Ra, the intensity of the flowing fluid is relatively weak, and the pressure is approximately identical in both sub-cavities, and therefore, the deformation of the flexible membrane is marginal.

The corresponding isotherms contours are presented in Figure 8. These contours demonstrate the variation of the heat transfer mechanism as Ra is varying. The isotherms tend to possess a stratification pattern as the Rayleigh number increases. This is the result of the augmentation of the strengthening of the convective currents as a result of the augmentation of the buoyancy forces. Additionally, Figure 8 states that at $Ra = 10^4$, the isotherms look mostly vertical, which is an indication to the dominance of the conduction mode against the convection one. As Ra increases, the impact of the conduction mechanism diminishes while the effect of the convection mode increases. In general, the onset of the buoyancy force dominance can be characterized when the isotherms are mostly horizontal and the membrane is deformed noticeably; this can be seen at $Ra = 10^6$.

Figures 9(a)-(b) and 10 show the evolution of the average Nusselt number Nu_{av}, average temperature T_{av} and the maximum stress σ_{max} for the flexible membrane. These figures are plotted for $Pr = 6.2$, $f = 10\pi$ and $E_\tau = 10^{13}$. The results are monitored after one cycle of the temperature oscillation ($\tau = 0.2$). From Figure 9(a) and (b), Nu_{av} (as a representation of the convective heat flux) and T_{av} vary in a sinusoidal fashion. The average Nusselt number doubles for each one order of magnitude of the Rayleigh number. Also, these figures show that an increase of Ra leads to an enhancement of the oscillation range of both Nu_{av} and T_{av}

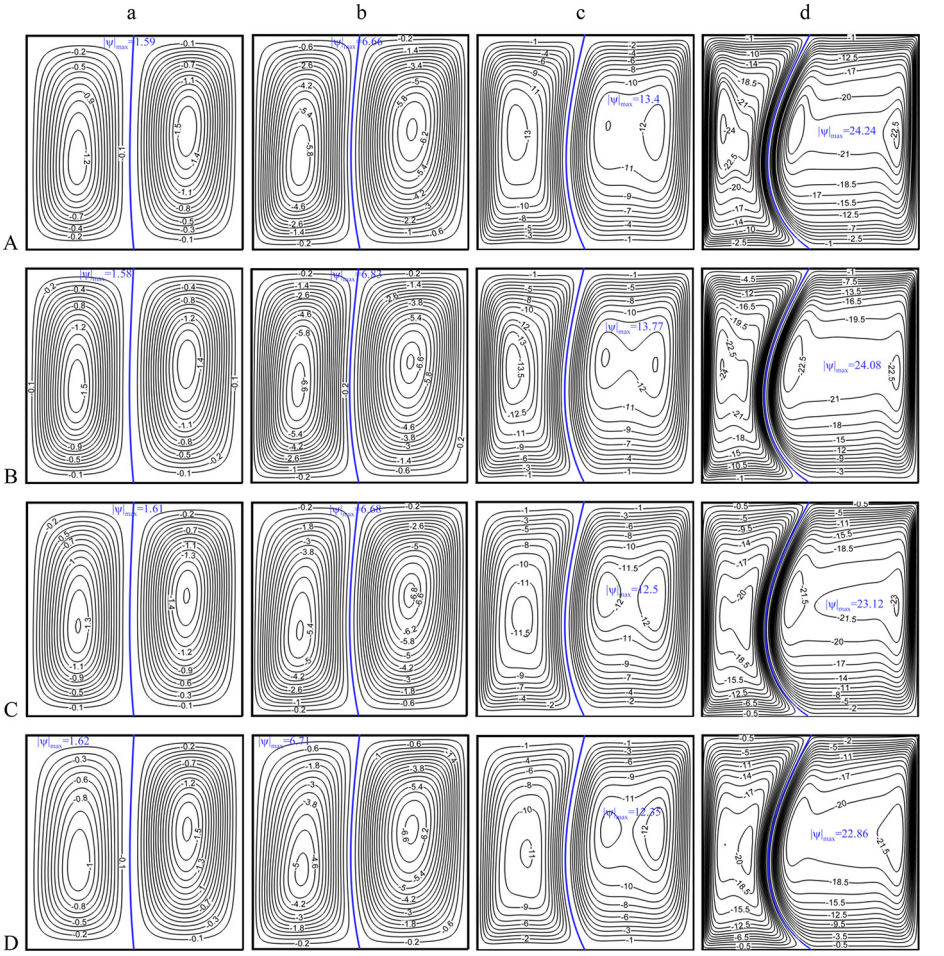

Figure 7.
Streamlines patterns for the cavities with Rayleigh numbers (a) $Ra = 10^4$, (b) $Ra = 10^5$, (c) $Ra = 10^6$ and (d) $Ra = 10^7$ in a period of oscillation (A: nT_p, B: $nT_p + T_p/4$, C: $nT_p + T_p/2$, D: $nT_p + 3T_p/4$) for $f = 10\pi$, $E_\tau = 10^{13}$ and $Pr = 6.2$

functions. Also, it is clear that with increasing *Ra*, the increased heat transfer rate Nu_{av} reduces T_{av}. Figure 10 illustrates that σ_{max} extremely enhances with an increase of *Ra*. In the case of $Ra = 10^4$, σ_{max} is almost constant. In this case, the maximum stress in the flexible membrane is in the order of 10^{10}, while it is clear that the oscillation function of σ_{max} is amplified as *Ra* increased. This can be attributed to the increasing deflection of the flexible membrane with *Ra*.

4.2 Effects of Prandtl number

The effects of Prandtl number (*Pr*) on the streamlines and isotherms contours in five periods of oscillation are displayed in Figures 11 and 12, respectively, for $Ra = 10^7$, $E_\tau = 10^{14}$, and $f = 10\pi$. Increasing the Prandtl number means increasing the momentum diffusion over the heat diffusion. As a result, it is clear from Figure 11 that in all periods of oscillation, the intensity of the flowing fluid increases with increasing values of Prandtl number, so that the

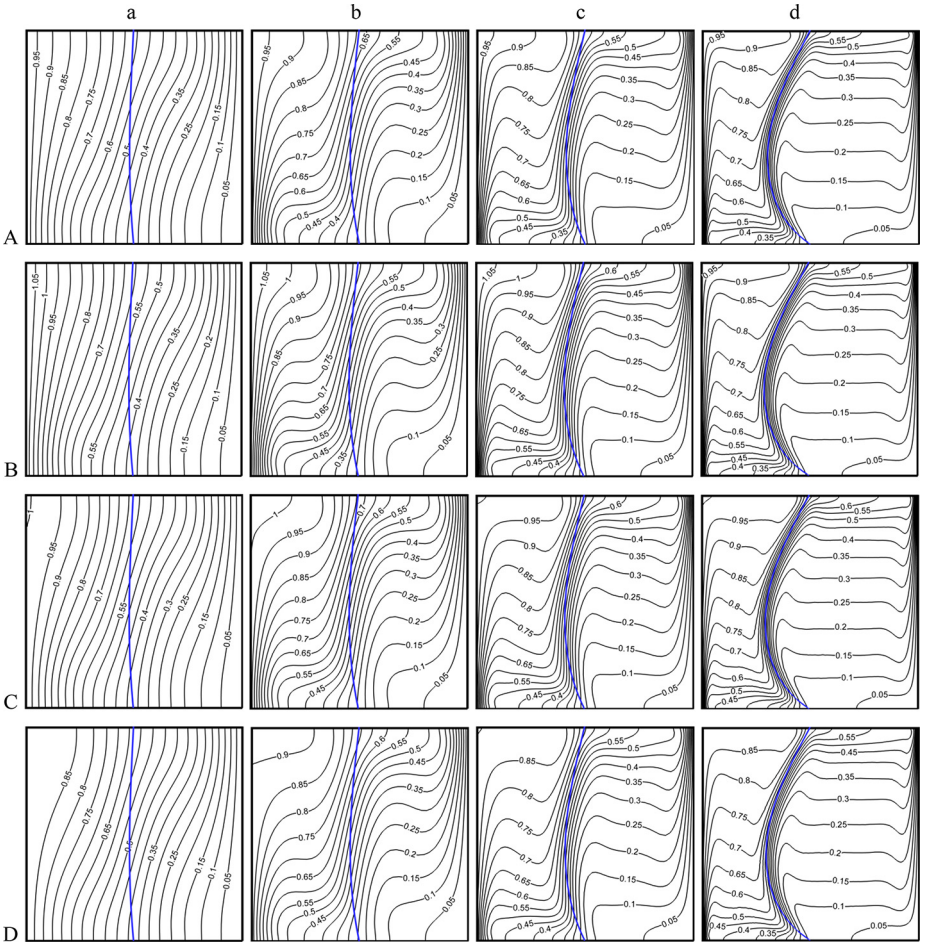

Figure 8.
Isotherms patterns for the cavities with Rayleigh numbers (a) $Ra = 10^4$, (b) $Ra = 10^5$, (c) $Ra = 10^6$ and (d) $Ra = 10^7$ in a period of oscillation (A: nT_p, B: $nT_p + T_p/4$, C: $nT_p + T_p/2$, D: $nT_p + 3T_p/4$) for $f = 10\pi$, $E_\tau = 10^{13}$ and $Pr = 6.2$

fluid interaction stretches the flexible membrane to the right. Also, it can be seen that the stretching of the flexible membrane grows slightly as time increases.

Figure 12 (whose parameters are the same as those labeled in Figure 11) shows that the isotherms follow the variations of the streamlines completely for all Prandtl numbers and times. In other words, the volumes of the warm (left) and cold (right) regions shrink and expand, respectively, as Prandtl number increases.

The variations of Nu_{av} and T_{av} inside the whole cavity are shown in Figure 13(a) and (b), respectively. For a better presentation of the results, the variations of Nu_{av} and T_{av} have been depicted in several periods of oscillation. As portrayed in Figure 13(a), the increase of Pr enhances the momentum exchange between the fluid molecules which in turn enhances the average Nusselt number Nu_{av}. In comparison with Pr = 0.71 (air), the amplitude of graphs with Pr = 6.2 (water) and Pr = 200 (engine oil) enhances 8.2 per cent and 22.5 per cent, respectively. According to these observations of Nu_{av}, Figure 13 (b) shows clearly that the T_{av} inside the whole enclosure decreases as Prandtl number increases. Here, unlike the

trend of the Nu_{av}, the sinusoidal graphs of the average temperature shift downwards and also, their amplitudes decrease with increasing values of Prandtl number. This reduction of the amplitude based on the amplitude of the sinusoidal function results for $Pr = 0.71$ equals 1.15 (with water) and 23.3 per cent (with engine oil).

The variations of the maximum stress σ_{max} in the flexible membrane versus the dimensionless time for several values of the Prandtl number are represented in Figure 14. The results state that the value of σ_{max} increases extremely when the Pr grows. The reason for this is the strengthening of fluid recirculation within the two sub-cavities. It is interesting to know that the enhancement of the amplitude of the sinusoidal variations of σ_{max} is 447.8 per cent and 15453 per cent for water and engine oil, respectively, compared with air.

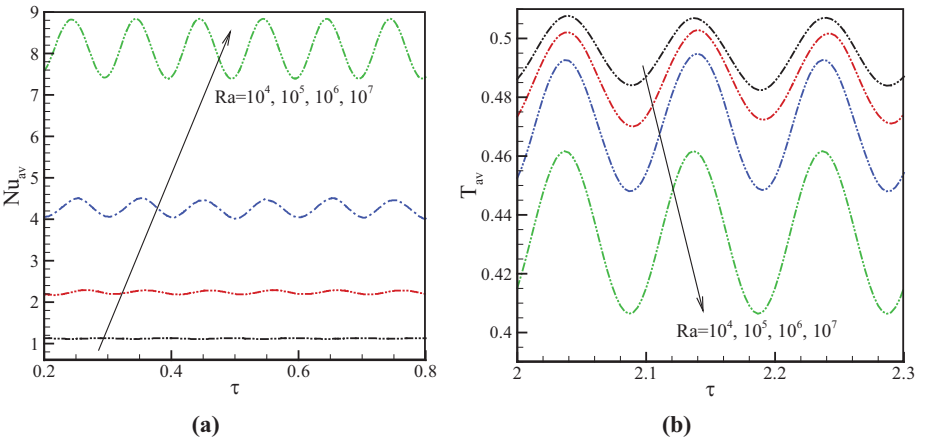

Figure 9.
Average Nusselt number (a) and the average temperature (b) versus dimensionless time for different values of Ra in $f = 10\pi$, $E_\tau = 10^{13}$ and $Pr = 6.2$

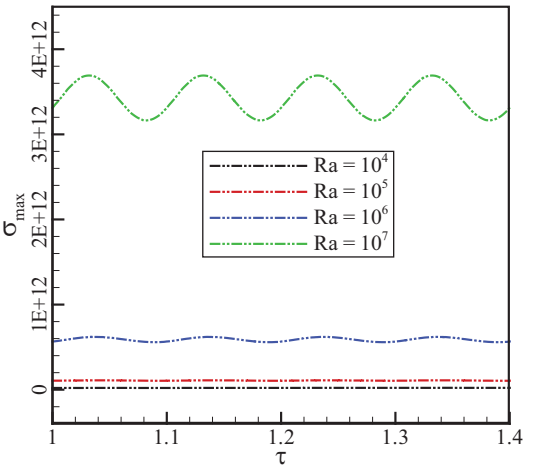

Figure 10.
The maximum stress in the flexible membrane versus dimensionless time for different values of Ra in $f = 10\pi$, $E_\tau = 10^{13}$ and $Pr = 6.2$

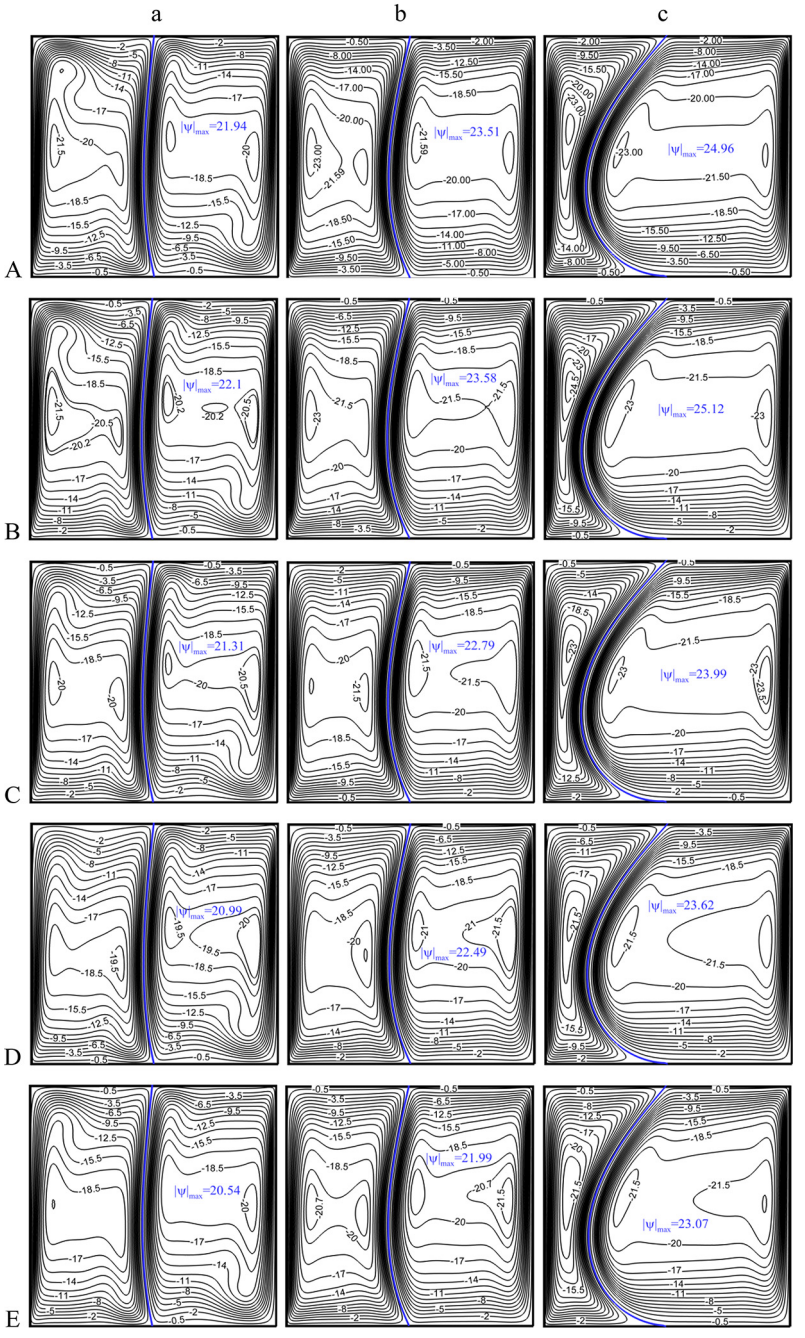

Figure 11.
Streamlines contours for Prandtl number a: $Pr = 0.71$ b: $Pr = 6.2$ and c: $Pr = 200$ in a period of oscillation (A: nT_p, B: $nT_p + T_p/5$, C: $nT_p + 2T_p/5$, D: $nT_p + 3T_p/5$, and E: $nT_p + 4T_p/5$) for $Ra = 10^7, f = 10\ \pi$ and $E_\tau = 10^{14}$

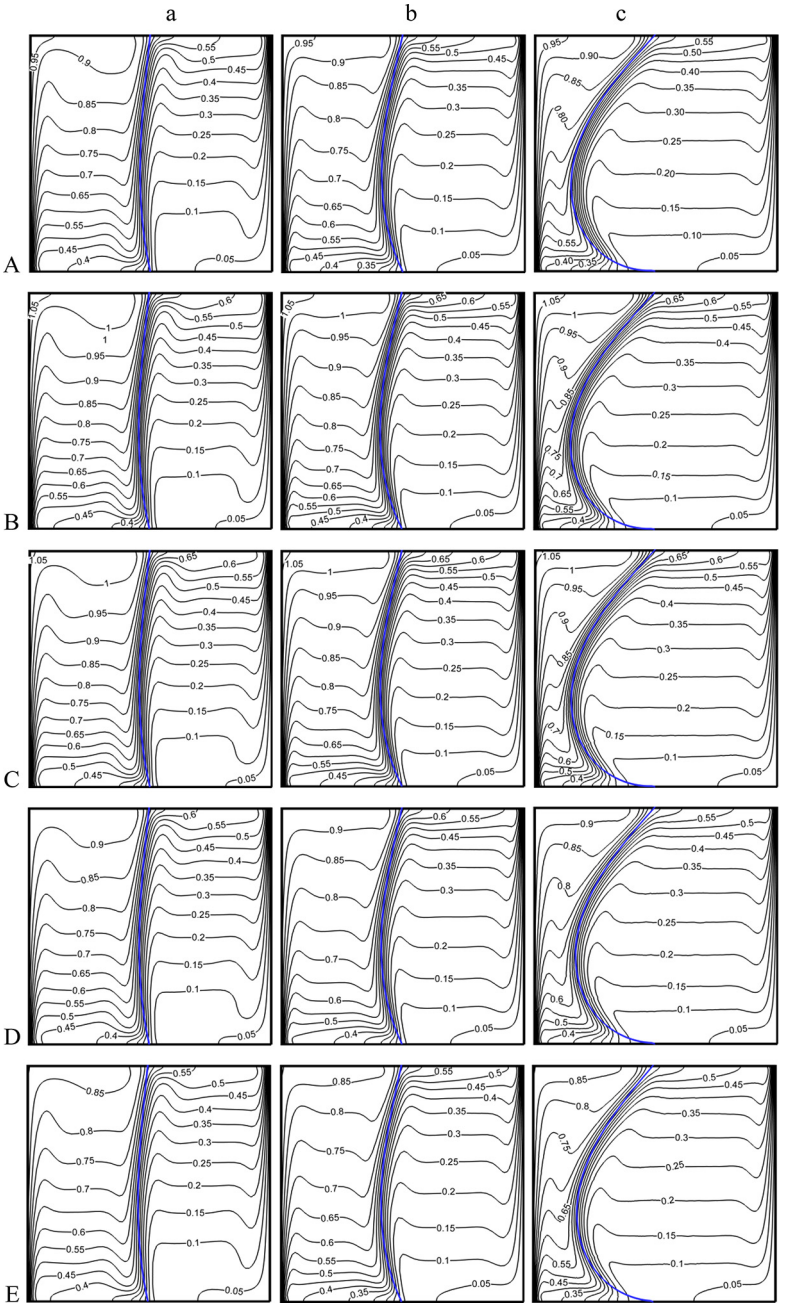

Figure 12.
Isotherm contours for Prandtl number (a) $Pr = 0.71$, (b) $Pr = 6.2$ and (c) $Pr = 200$ in a period of oscillation (A: nT_p, B: $nT_p + T_p/5$, C: $nT_p + 2T_p/5$, D: $nT_p + 3T_p/5$, E: $nT_p + 4T_p/5$) for $Ra = 10^7$, $f = 10\pi$ and $E_\tau = 10^{14}$

4.3 Effects of the temperature oscillation frequency

Figures 15 and 16 illustrate the efficacies of the oscillating temperature frequency on the flow and temperature fields, respectively, while the other parameters are fixed at $Ra = 10^7$, $E_\tau = 10^{14}$ and $Pr = 6.2$. As can be observed from the streamlines' patterns, the frequency influences the strength of the fluid flow, while the patterns of the streamlines are indiscernible. Also, there are no noticeable variations in the streamlines trend with different times. At a specific time, the frequency increases the strength of flow ($\tau = T_p$), while at another time, there is no certain trend (for example, $\tau = T_p + 3T_p/4$). According to the corresponding isotherms (Figure. 16), we conclude that in the left sub-cavity, the isotherms move up with the frequency when $\tau = T_p$ and $T_p + T_p/4$, while if τ is $nT_p + T_p/2$ or $nT_p + 3T_p/4$, the isotherms shift downward as the frequency augments.

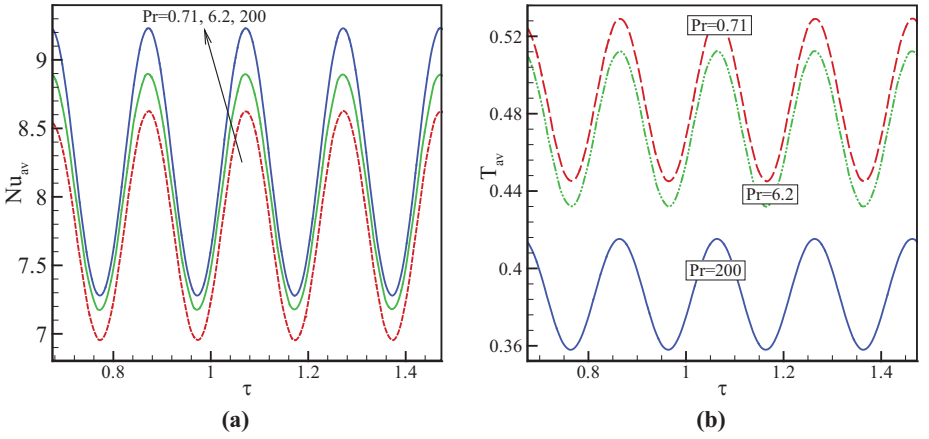

Figure 13. The average Nusselt number on the right wall (a) and the average temperature inside whole cavity (b) for different periods of oscillation with Prandtl number $Pr = 0.71$, 6.2 and 200 for $Ra = 10^7$, $f = 10\pi$ and $E_\tau = 10^{14}$

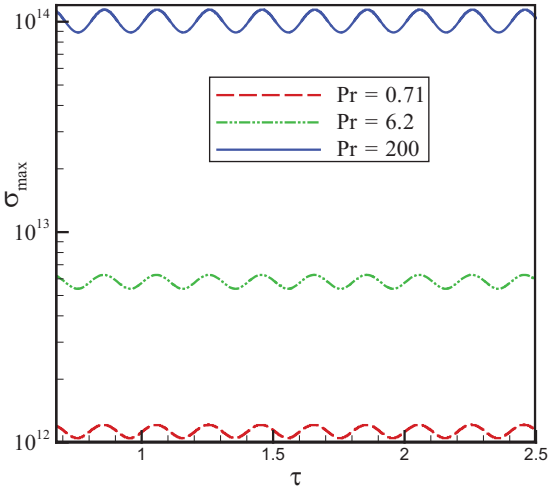

Figure 14. Maximum stress σ_{max} according to dimensionless time for the different values of Pr in $Ra = 10^7$, $f = 10\pi$ and $E_\tau = 10^{14}$

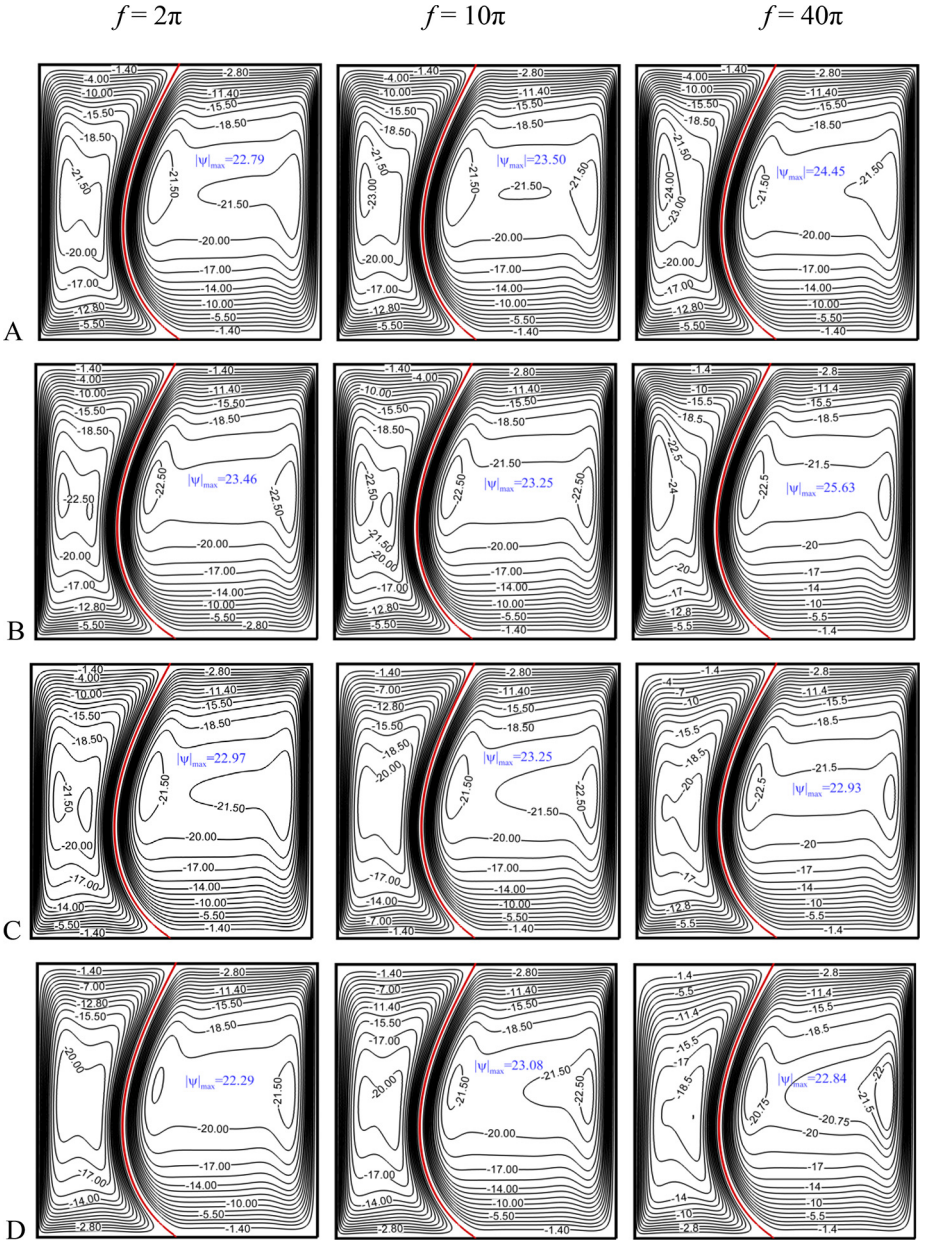

Figure 15.
Streamline contours for the different values of frequency in different periods of oscillation (A: nT_p, B: $nT_p + T_p/4$, C: $nT_p + T_p/2$, D: $nT_p + 3T_p/4$) for $Ra = 10^7$, $Pr = 6.2$ and $E_\tau = 10^{14}$

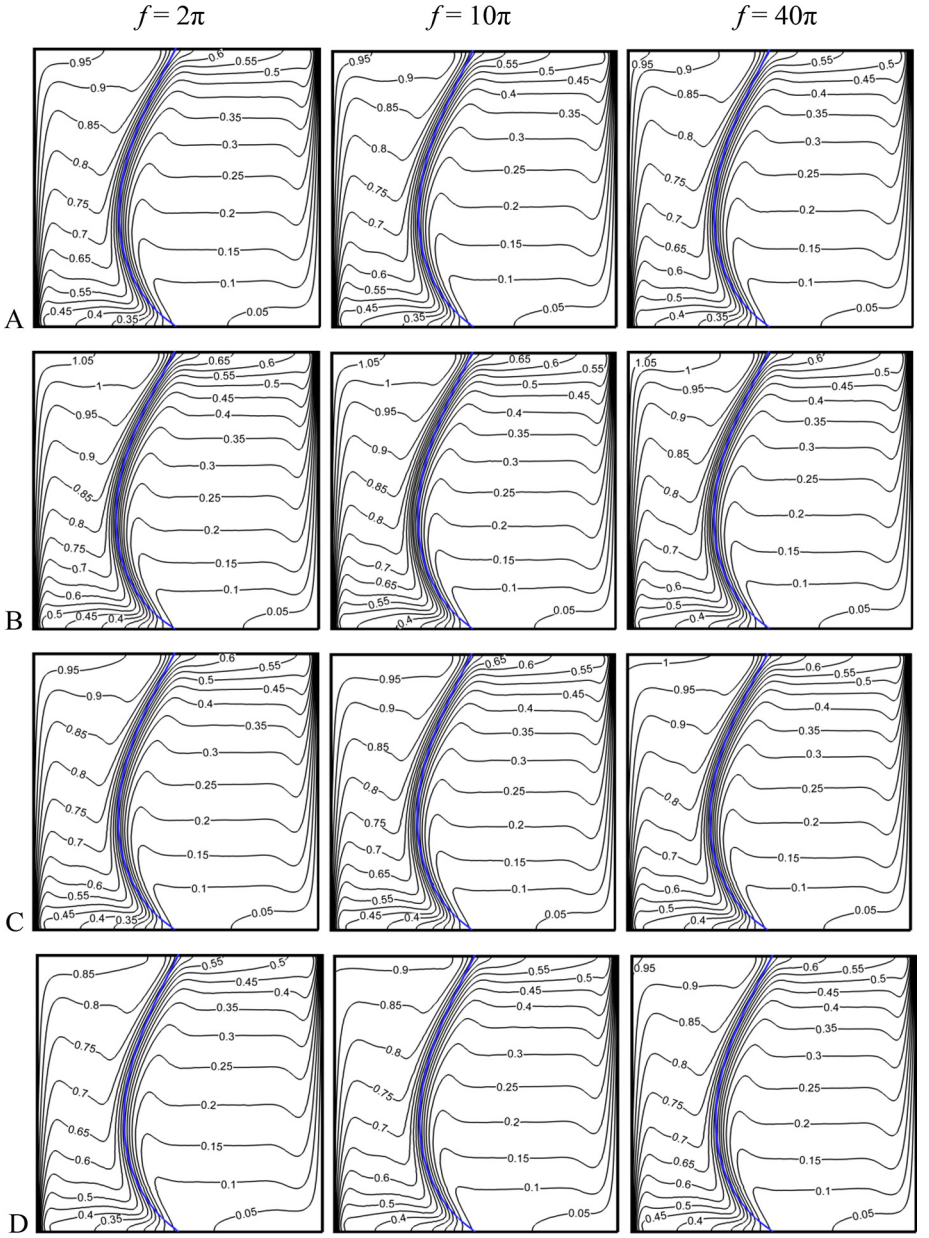

Figure 16.
Isotherms contours for different frequency values and different periods of oscillation (A: nT_p, B: $nT_p + T_p/4$, C: $nT_p + T_p/2$, D: $nT_p + 3T_p/4$) for $Ra = 10^7$, $Pr = 6.2$ and $E_\tau = 10^{14}$

From Figures 17 (a) and (b), obviously, the frequency increment decreases both the amplitude of the Nu_{av} and T_{av} for $Ra = 10^7$, $Pr = 6.2$ and $E_\tau = 10^{14}$. The Nusselt number and the average temperature time functions for all frequency values oscillate around certain values which are 8.1 and 0.435, respectively. Therefore, it can be concluded that the frequency influences only the amplitude of the Nu_{av} and T_{av} as time functions and has no effect on the period-averaged Nu_{av} and T_{av}. The graph of the maximum stress in the flexible membrane shown in Figure 18 also follows the trend of Nu_{av} and T_{av} with the frequency. Accordingly, it seems that when f tends to infinity, the amplitude of the oscillatory functions mentioned approaches constant values. Physically, when f tends to infinity, the left wall temperature oscillates very quickly so that the fluid does not have enough time to receive the temperature oscillation effects.

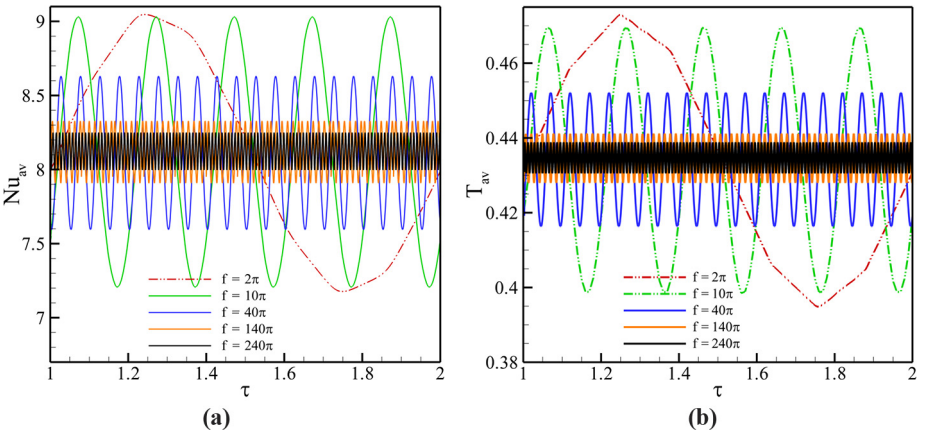

Figure 17.
Variations of (a) average Nusselt number Nu_{av} and (b) average temperature T_{av} versus dimensionless time for the different values of frequency in $Ra = 10^7$, $Pr = 6.2$, and $E_\tau = 10^{14}$

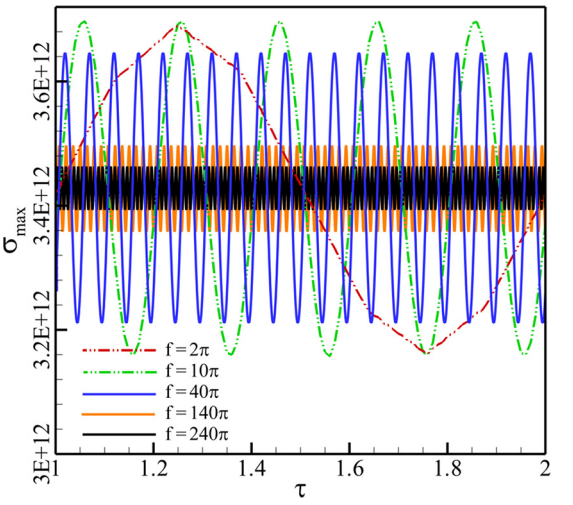

Figure 18.
Variations σ_{max} according to dimensionless time for the different values of frequency in $Ra = 10^7$, $Pr = 6.2$ and $E_\tau = 10^{14}$

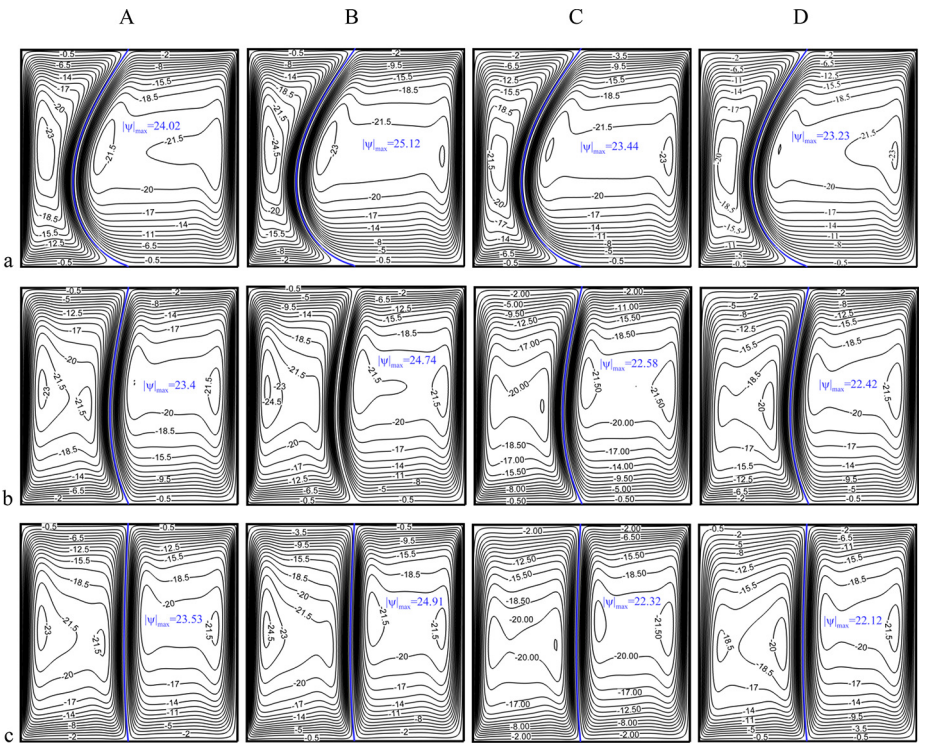

Figure 19. Streamlines for the cavities with modulus elasticity (a) $E_\tau = 5 \times 10^{12}$, (b) $E_\tau = 10^{14}$ and (c) $E_\tau = 10^{16}$ in different periods of oscillation (A: nT_p, B: $nT_p + T_p/4$, C: $nT_p + T_p/2$, D: $nT_p + 3T_p/4$) for $Ra = 10^7$, $f = 20\pi$ and $Pr = 6.2$

4.4 Effects of elasticity modulus

The thermal and dynamical behaviors of the fluid under the influence of the variation of the elasticity modulus are presented in Figures 19 and 20. In these figures, each of the vertical columns illustrates the flow and temperature fields at a specific time. For all elasticity modulus values, the intensified fluid flow occurs in the second column, at a period of oscillation equals to $nT_p + T_p/4$. For a low value of the elasticity modulus, the flexible membrane experiences substantial deformation when faster circulated fluid exerts larger forces; as such, the highest flexible membrane stretching is noticed for the lower values of the elasticity modulus. The stretched membrane results in a substantial space available for the right sub-cavity; thus, the highest fluid flow intensity is recorded for the lower elasticity modulus. The vortex created in the left part of the enclosure for the lowest elasticity modulus ($E_\tau = 5 \times 10^{12}$) case breaks into two vortices when E_τ changes from $E_\tau = 5 \times 10^{12}$ to $E_\tau = 10^{13}$. After that, the general patterns of the streamlines are the same for all values of the elasticity modulus. Figure 20 shows that the isotherms contours are formed following the streamline patterns. Among the times defined for displaying the streamlines and the isotherms, the maximum temperature is observed at $nT_p + T_p/4$.

Figure 21(a) and (b) displays the variations of Nu_{av} and T_{av} versus several periods of oscillation for different values of E_τ. In general, it can be stated that the Nu_{av} was decreased and T_{av} was augmented by the increase of the elasticity modulus. However, it should be noted that the reduction and augmentation rate of Nu_{av} and T_{av} decay when the value of E_τ is higher than $E_\tau = 10^{14}$. To justify these behaviors, it can be said that

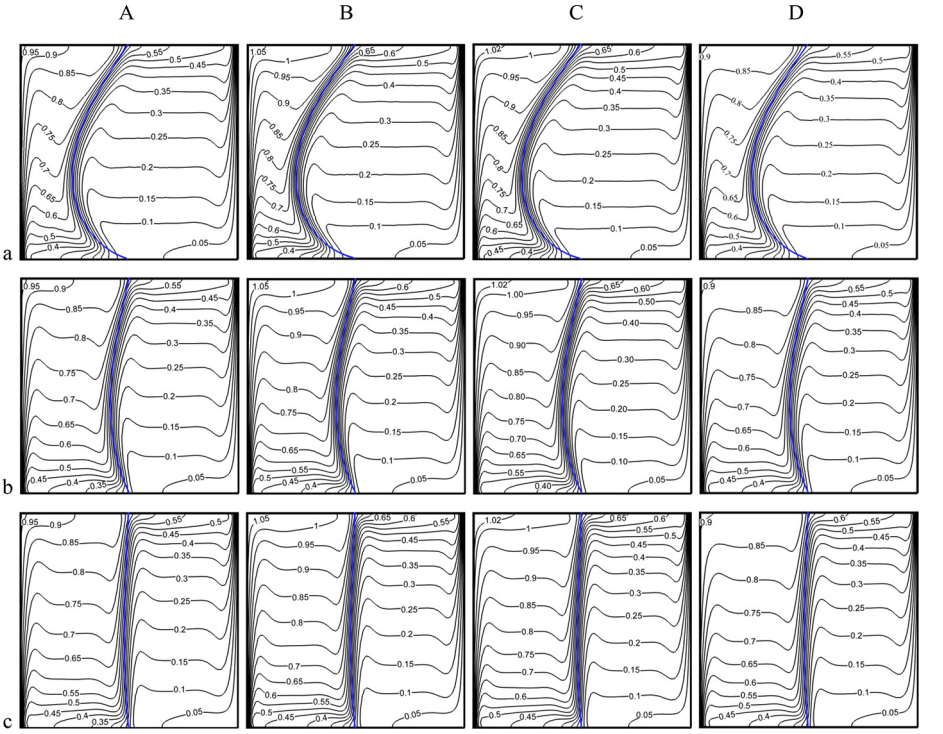

Figure 20.
Isotherms contours for the cavities with modulus elasticity a: $E_\tau = 5 \times 10^{12}$, b: $E_\tau = 10^{14}$ and c: $E_\tau = 10^{16}$ in different periods of oscillation (A: nT_p, B: $nT_p + T_p/4$, C: $nT_p + T_p/2$, D: $nT_p + 3T_p/4$) for $Ra = 10^7$, $f = 20\pi$ and $Pr = 6.2$

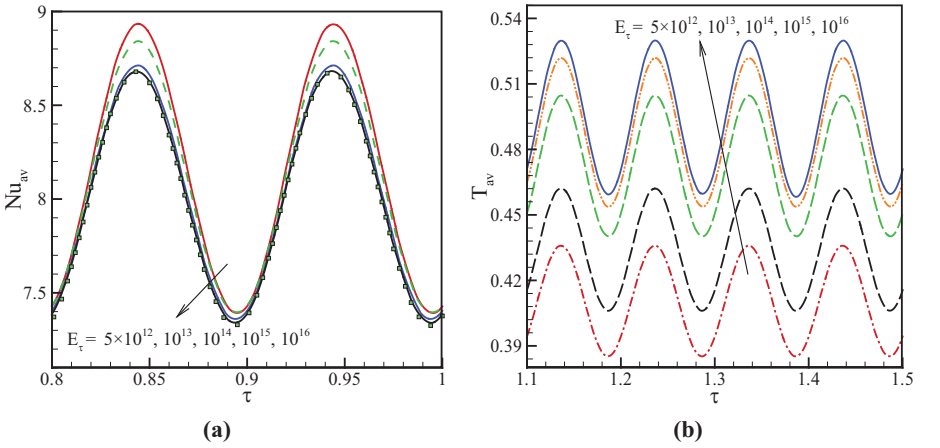

Figure 21.
Variations of Nu_{av} (a) and T_{av} (b) versus oscillation period for different values of E_τ at $Ra = 10^7$, $f = 20\pi$ and $Pr = 6.2$

when the elasticity modulus of the membrane is low, an interaction between the solid material and the fluid takes place, the movement of the membrane is easier and more in a period of oscillation; hence, some fluid exits from the embedded eyelets. Some cold and fresh fluid substitutes this quantity of fluid. In contrast, when the elasticity

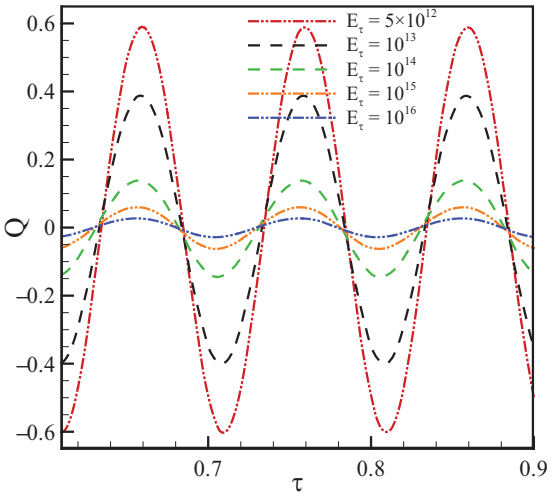

Figure 22. Dimensionless flow rate through the left embedded eyelet versus oscillation period for different values of E_τ at $Ra = 10^7$, $f = 20\pi$ and $Pr = 6.2$

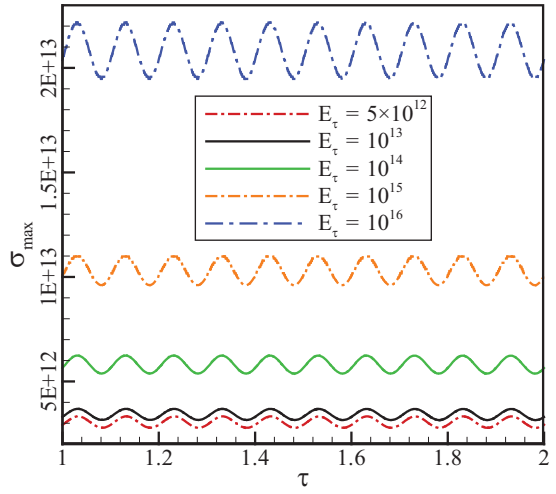

Figure 23. Variations of σ_{max} versus oscillation period for different values of E_τ at $Ra = 10^7$, $f = 20\pi$ and $Pr = 6.2$

modulus is high, the deflection of the flexible partition is restricted; consequently, the fluid entry and exit cannot be seen significantly. This claim is proven by the representation of the discharge or charge of the enclosure through the eyelets in Figure 22. In Figure 22, Q is the dimensionless flow rate through the left eyelet. The negative and positive values of Q depict the intake and the discharge of the fluid through the eyelets.

Finally, Figure 23 provides information about the variations of σ_{max} versus the oscillation period for different values of E_τ when $Ra = 10^7$, $f = 10\pi$ and $Pr = 6.2$. The obtained results show a noticeable increase in the maximum stress in the membrane σ_{max} with the increase of E_τ. This is because the increase of the elasticity modulus gives rise to

the stiffness of the membrane wall, which in turn leads to much high resistance against the force exerted by the fluid circulation. Besides, the oscillation amplitude of σ_{max} increases as E_τ is increased.

5. Conclusions

The investigated problem in this work is a fluid–structure interaction (FSI) representing a periodically heated square cavity divided vertically into half by a flexible membrane. The left vertical wall is exposed to a sinusoidal time-varying temperature, while the right surface is kept isothermal at a cold temperature. There is no thermal diffusion from the upper and lower horizontal boundaries. The interdependent, complex and non-linear governing equations are solved by using the Galerkin finite element approach with the aid of ALE technique. Four pertinent parameters are altered in this study. According to these studied parameters, the following concluding remarks are drawn:

- Owing to the applied boundary conditions, the general behavior of the flexible partition is stretched to the left, resulting in shrinking the left sub-cavity and expanding the right one.
- A fluid with a high Prandtl number enhances the convective heat transfer and robustly stretches the flexible membrane, and as a result, the associated maximum stress increases.
- The lower the elasticity modulus of the flexible membrane is, the higher are the flexible partition deflection, mean Nusselt number and the maximum stress of the partition.
- The frequency of the oscillating left wall temperature does not affect the deformation and the stress of the flexible membrane, the $Nu_{av,}$ and T_{av}. Nevertheless, the amplitudes of Nu_{av}, T_{av} and σ_{max} are decreasing functions of the wall temperature frequency.
- The periodic state values of both Nu_{av} and σ_{max} of the flexible partition increase significantly with the increase of Ra.

In the present study, as a pioneer study, the membrane was modeled as a flexible thin divider, and the effects of membrane permeability, porosity and extra layers are neglected. Modeling the membrane with more details can be subject of future studies.

References

Abouali, O. and Falahatpisheh, A. (2009), "Numerical investigation of natural convection of Al2O3 nanofluid in vertical annuli", *Heat and Mass Transfer*, Vol. 46 No. 1, p. 15.

Alsabery, A., Chamkha, A., Hashim, I. and Siddheshwar, P. (2017), "Effects of nonuniform heating and wall conduction on natural convection in a square porous cavity using LTNE model", *Journal of Heat Transfer*, Vol. 139 No. 12, p. 122008.

Alsabery, A., Sheremet, M., Chamkha, A. and Hashim, I. (2018a), "Conjugate natural convection of Al2O3–water nanofluid in a square cavity with a concentric solid insert using Buongiorno's two-phase model", *International Journal of Mechanical Sciences*, Vol. 136, pp. 200-219.

Alsabery, A., Sheremet, M., Chamkha, A. and Hashim, I. (2018b), "MHD convective heat transfer in a discretely heated square cavity with conductive inner block using two-phase nanofluid model", *Scientific Reports*, Vol. 8 No. 1, p. 7410.

Alsabery, A., Sheremet, M., Chamkha, A. and Hashim, I. (2019), "Impact of nonhomogeneous nanofluid model on transient mixed convection in a double lid-driven wavy cavity involving solid circular cylinder", *International Journal of Mechanical Sciences*, Vol. 150, pp. 637-655.

Alsabery, A., Yazdi, M., Altawallbeh, A. and Hashim, I. (2018d), "Effects of nonhomogeneous nanofluid model on convective heat transfer in partially heated square cavity with conducting solid block", *Journal of Thermal Analysis and Calorimetry*, Vol. 136 No. 4, pp. 1489-1514.

Alsabery, A., Sheremet, M., Ghalambaz, M., Chamkha, A. and Hashim, I. (2018c), "Fluid-structure interaction in natural convection heat transfer in an oblique cavity with a flexible oscillating fin and partial heating", *Applied Thermal Engineering*, Vol. 145, pp. 80-97.

Astanina, M.S., Sheremet, M. and Umavathi, C.J. (2018), "Unsteady natural convection in a partially porous cavity having a heat-generating source using local thermal non-equilibrium model", *International Journal of Numerical Methods for Heat and Fluid Flow*, available at: https://doi.org/10.1108/HFF-06-2018-0338

Baïri, A., Zarco-Pernia, E. and De María, J.-M.G. (2014), "A review on natural convection in enclosures for engineering applications. The particular case of the parallelogrammic diode cavity", *Applied Thermal Engineering*, Vol. 63 No. 1, pp. 304-322.

Basak, T. and Chamkha, A.J. (2012), "Heatline analysis on natural convection for nanofluids confined within square cavities with various thermal boundary conditions", *International Journal of Heat and Mass Transfer*, Vol. 55 Nos 21/22, pp. 5526-5543.

Bondareva, N.S. and Sheremet, M.A. (2018), "Conjugate heat transfer in the PCM-based heat storage system with finned copper profile: application in electronics cooling", *International Journal of Heat and Mass Transfer*, Vol. 124, pp. 1275-1284.

Bondarenko, D.S., Sheremet, M.A., Oztop, H.F. and Ali, M.E. (2019), "Impacts of moving wall and heat-generating element on heat transfer and entropy generation of Al 2 O 3/H 2 O nanofluid", *Journal of Thermal Analysis and Calorimetry*, Vol. 136 No. 2, pp. 673-686.

Cassard, H.M. and Park, H.G.J.J.O.M.S. (2018), "How to select the optimal membrane distillation system for industrial applications", *Journal of Membrane Science*, Vol. 565, pp. 402-410.

Chamkha, A.J. and Ismael, M.A. (2014), "Natural convection in differentially heated partially porous layered cavities filled with a nanofluid", *Numerical Heat Transfer, Part A: Applications*, Vol. 65 No. 11, pp. 1089-1113.

Churchill, S. (1983), "Free convection in layers and enclosures", *Heat Exchanger Design Handbook*, Vol. 2, doi: 10.1615/hedhme.a.000175.

De Almeida, V.F. and Hart, K.J.J.J.O.M.S. (2017), "Analysis of gas membrane ultra-high purification of small quantities of Mono-isotopic silane", *Journal of Membrane Science*, Vol. 527, pp. 164-179.

De Nayer, G. and Breuer, M. (2014), "Numerical FSI investigation based on LES: flow past a cylinder with a flexible splitter plate involving large deformations (FSI-PfS-2a)", *International Journal of Heat and Fluid Flow*, Vol. 50, pp. 300-315.

Donea, J. and Huerta, A. (2003), *Finite Element Methods for Flow Problems*, John Wiley and Sons, Hoboken, NJ.

Engel, M. and Griebel, M. (2006), "Flow simulation on moving boundary-fitted grids and application to fluid–structure interaction problems", *International Journal for Numerical Methods in Fluids*, Vol. 50 No. 4, pp. 437-468.

Feng, S., Li, D., Low, Z.-X., Liu, Z., Zhong, Z., Hu, Y., Wang, Y. and Xing, W.J.J.O.M.S. (2017), "ALD-seeded hydrothermally-grown Ag/ZnO nanorod PTFE membrane as efficient indoor air filter", *Journal of Membrane Science*, Vol. 531, pp. 86-93.

Fu, W.-S. and Huang, C.-P. (2006), "Effects of a vibrational heat surface on natural convection in a vertical channel flow", *International Journal of Heat and Mass Transfer*, Vol. 49 Nos. 7/8, pp. 1340-1349.

Ghalambaz, M., Jamesahar, E., Ismael, M.A. and Chamkha, A.J. (2017), "Fluid-structure interaction study of natural convection heat transfer over a flexible oscillating fin in a square cavity", *International Journal of Thermal Sciences*, Vol. 111, pp. 256-273.

Ghalambaz, M., Sheremet, M.A., Mehryan, S.A.M., Kashkooli, F.M. and Pop, I. (2018), "Local thermal non-equilibrium analysis of conjugate free convection within a porous enclosure occupied with Ag–MgO hybrid nanofluid", *Journal of Thermal Analysis and Calorimetry*, Vol. 135 No. 2, pp. 1381-1398.

Jamesahar, E., Ghalambaz, M. and Chamkha, A.J. (2016), "Fluid–solid interaction in natural convection heat transfer in a square cavity with a perfectly thermal-conductive flexible diagonal partition", *International Journal of Heat and Mass Transfer*, Vol. 100, pp. 303-319.

Jang, S., Yoon, Y.-G., Lee, Y.-S. and Choi, Y.-W.J.J.O.M.S. (2018), "One-step fabrication and characterization of reinforced microcomposite membranes for polymer electrolyte membrane fuel cells", *Journal of Membrane Science*, Vol. 563, pp. 896-902.

Kahveci, K. (2007), "Natural convection in a partitioned vertical enclosure heated with a uniform heat flux", *Journal of Heat Transfer*, Vol. 129 No. 6, pp. 717-726.

Kalabin, E., Kanashina, M. and Zubkov, P. (2005), "Natural-convective heat transfer in a square cavity with time-varying side-wall temperature", *Numerical Heat Transfer, Part A: Applications*, Vol. 47 No. 6, pp. 621-631.

Kalmbach, A. and Breuer, M. (2013), "Experimental PIV/V3V measurements of vortex-induced fluid–structure interaction in turbulent flow – a new benchmark FSI-PfS-2a", *Journal of Fluids and Structures*, Vol. 42, pp. 369-387.

Küttler, U. and Wall, W.A. (2008), "Fixed-point fluid–structure interaction solvers with dynamic relaxation", *Computational Mechanics*, Vol. 43 No. 1, pp. 61-72.

Lee, J., Shin, J. and Lee, S. (2012), "Fluid–structure interaction of a flapping flexible plate in quiescent fluid", *Computers and Fluids*, Vol. 57, pp. 124-137.

Markatos, N.C. and Pericleous, K. (1984), "Laminar and turbulent natural convection in an enclosed cavity", *International Journal of Heat and Mass Transfer*, Vol. 27 No. 5, pp. 755-772.

Mehryan, S., Chamkha, A., Ismael, M. and Ghalambaz, M. (2017a), "Fluid–structure interaction analysis of free convection in an inclined square cavity partitioned by a flexible impermeable membrane with sinusoidal temperature heating", *Meccanica*, Vol. 52 Nos. 11/12, pp. 2685-2703.

Mehryan, S., Ghalambaz, M., Ismael, M.A. and Chamkha, A.J. (2017b), "Analysis of fluid-solid interaction in MHD natural convection in a square cavity equally partitioned by a vertical flexible membrane", *Journal of Magnetism and Magnetic Materials*, Vol. 424, pp. 161-173.

Mehryan, S., Ghalambaz, M. and Izadi, M. (2019), "Conjugate natural convection of nanofluids inside an enclosure filled by three layers of solid, porous medium and free nanofluid using Buongiorno's and local thermal non-equilibrium models", *Journal of Thermal Analysis and Calorimetry*, Vol. 135 No. 2, pp. 1047-1067.

Mehryan, S., Izadpanahi, E., Ghalambaz, M. and Chamkha, A. (2019a), " Mixed convection flow caused by an oscillating cylinder in a square cavity filled with Cu–Al 2 O 3/water hybrid nanofluid", *Journal of Thermal Analysis and Calorimetry*, in press, pp. 1-18, available at: https://doi.org/10.1007/s10973-019-08012-2

Mehryan, S., Sheremet, M.A., Soltani, M. and Izadi, M. (2019b), "Natural convection of magnetic hybrid nanofluid inside a double-porous medium using two-equation energy model", *Journal of Molecular Liquids*, Vol. 277, pp. 959-970.

Miroshnichenko, I.V., Sheremet, M.A., Oztop, H.F. and Abu-Hamdeh, N. (2018), "Natural convection of alumina-water nanofluid in an open cavity having multiple porous layers", *International Journal of Heat and Mass Transfer*, Vol. 125, pp. 648-657.

Nishimura, T., Shiraishi, M., Nagasawa, F. and Kawamura, Y. (1988), "Natural convection heat transfer in enclosures with multiple vertical partitions", *International Journal of Heat and Mass Transfer*, Vol. 31 No. 8, pp. 1679-1686.

Ogden, R.W. (1997), *Non-Linear Elastic Deformations*, Courier Corporation, North Chelmsford, Chelmsford.

Oztop, H.F., Varol, Y. and Koca, A. (2009), "Natural convection in a vertically divided square enclosure by a solid partition into air and water regions", *International Journal of Heat and Mass Transfer*, Vol. 52 Nos. 25/26, pp. 5909-5921.

Sadiq, M., Alsabery, A. and Hashim, I. (2018), "MHD mixed convection in a lid-driven cavity with a bottom trapezoidal body: two-phase nanofluid model", *Energies*, Vol. 11 No. 11, p. 2943.

Sheikholeslami, M., Mehryan, S.A.M., Shafee, A. and Sheremet, M.A. (2019), "Variable magnetic forces impact on magnetizable hybrid nanofluid heat transfer through a circular cavity", *Journal of Molecular Liquids*, Vol. 277, pp. 388-396.

Sheremet, M.A., Oztop, H.F., Gvozdyakov, D.V. and Ali, M.E. (2018), "Impacts of heat-conducting solid wall and heat-generating element on free convection of Al 2 O 3/H 2 O nanofluid in a cavity with open border", *Energies*, Vol. 11, pp. 1-17.

Süli, E. and Mayers, D.F. (2003), *An Introduction to Numerical Analysis*, Cambridge university press, Cambridge.

Tahmasebi, A., Mahdavi, M. and Ghalambaz, M. (2018), "Local thermal nonequilibrium conjugate natural convection heat transfer of nanofluids in a cavity partially filled with porous media using Buongiorno's model", *Numerical Heat Transfer, Part A: Applications*, Vol. 73 No. 4, pp. 254-276.

Tatsuo, N., Mitsuhiro, S. and Yuji, K. (1987), "Natural convection heat transfer in enclosures with an off-center partition", *International Journal of Heat and Mass Transfer*, Vol. 30 No. 8, pp. 1756-1758.

van Loon, R., Anderson, P., van de Vosse, F. and Sherwin, S. (2007), "Comparison of various fluid–structure interaction methods for deformable bodies", *Computers and Structures*, Vol. 85, pp. 833-843.

Varol, Y., Oztop, H.F. and Pop, I. (2009), "Natural convection in a diagonally divided square cavity filled with a porous medium", *International Journal of Thermal Sciences*, Vol. 48 No. 7, pp. 1405-1415.

Xie, Y., Zou, H., Xiang, H., Xia, R., Liang, D., Shi, P., Dai, S. and Wang, H.J.J.O.M.S. (2016), "Enhancement on the wettability of lithium battery separator toward nonaqueous electrolytes", *Journal of Membrane Science*, Vol. 503, pp. 25-30.

Xu, F., Patterson, J.C. and Lei, C. (2009), "Heat transfer through coupled thermal boundary layers induced by a suddenly generated temperature difference", *International Journal of Heat and Mass Transfer*, Vol. 52 No. 21-22, pp. 4966-4975.

Zargartalebi, H., Ghalambaz, M., Chamkha, A., Pop, I. and Nezhad, A.S. (2018), "Fluid-structure interaction analysis of buoyancy-driven fluid and heat transfer through an enclosure with a flexible thin partition", *International Journal of Numerical Methods for Heat and Fluid Flow*, Vol. 28, pp. 2072-2088.

Corresponding authors
Mohammad Ghalambaz can be contacted at: mohammad.ghalambaz@tdtu.edu.vn and D. Wen can be contacted at: d.wen@buaa.edu.cn and d.wen@leeds.ac.uk